Effects of Ocean Biology on the Penetrative Radiation in a Coupled Climate Model

PATRICK WETZEL, ERNST MAIER-REIMER, MICHAEL BOTZET, AND JOHANN JUNGCLAUS

Max Planck Institute for Meteorology, Hamburg, Germany

NOEL KEENLYSIDE AND MOJIB LATIF

IfM GEOMAR, Leibniz-Institut für Meereswissenschaften, Kiel, Germany

(Manuscript received 20 December 2004, in final form 2 November 2005)

ABSTRACT

The influence of phytoplankton on the seasonal cycle and the mean global climate is investigated in a fully coupled climate model. The control experiment uses a fixed attenuation depth for shortwave radiation, while the attenuation depth in the experiment with biology is derived from phytoplankton concentrations simulated with a marine biogeochemical model coupled online to the ocean model. Some of the changes in the upper ocean are similar to the results from previous studies that did not use interactive atmospheres, for example, amplification of the seasonal cycle; warming in upwelling regions, such as the equatorial Pacific and the Arabian Sea; and reduction in sea ice cover in the high latitudes. In addition, positive feedbacks within the climate system cause a global shift of the seasonal cycle. The onset of spring is about 2 weeks earlier, which results in a more realistic representation of the seasons. Feedback mechanisms, such as increased wind stress and changes in the shortwave radiation, lead to significant warming in the midlatitudes in summer and to seasonal modifications of the overall warming in the equatorial Pacific. Temperature changes also occur over land where they are sometimes even larger than over the ocean. In the equatorial Pacific, the strength of interannual SST variability is reduced by about 10%–15% and phase locking to the annual cycle is improved. The ENSO spectral peak is broader than in the experiment without biology and the dominant ENSO period is increased to around 5 yr. Also the skewness of ENSO variability is slightly improved. All of these changes lead to the conclusion that the influence of marine biology on the radiative budget of the upper ocean should be considered in detailed simulations of the earth's climate.

1. Introduction

About half of the solar energy is within the spectral range of 350 to 700 nm, where pure seawater is highly transparent. Marine phytoplankton absorb light within this spectral range and thereby modulate the heat flux in the upper ocean (Morel 1988; Morel and Maritorena 2001). The magnitude and variability of the solar radiation flux through the upper-ocean layers has been investigated for various ocean regions (Ohlmann et al. 2000; Ohlmann and Siegel 2000). Light absorption by phytoplankton has potential implication for biological and physical processes as well as for ocean–atmosphere interactions. Ocean transports are influenced by the redistribution of heat, especially the partitioning of heat between the mixed layer and the deep ocean. Temperature changes, in turn, alter the dynamical turbulence in the ocean and the mixed layer depth. Sea–air heat and moisture fluxes are regulated by the surface ocean temperature. Furthermore, marine biology is itself affected by dynamical and temperature changes. Enhanced stratification can lead to better growth conditions for phytoplankton, while changes in mixing and upwelling may alter the amount of nutrients available. Limited growth in deeper layers due to self-shading is another process that can be addressed in a coupled ecosystem model.

Previous studies focused on the tropical oceans. Observational evidence for a significant role of phytoplankton concentration for the upper-ocean heat budget in the equatorial Pacific is reported by Siegel et al. (1995), Chavez et al. (1998), and Strutton and Chavez (2004). Murtugudde et al. (2002) have tested possible effects on the upper tropical ocean circulation in an ocean general circulation model (GCM). Nakamoto et

Corresponding author address: Dr. Johann Jungclaus, Max Planck Institute for Meteorology, Bundesstrasse 53, 20146 Hamburg, Germany.
E-mail: johannjungclaus@zmaw.de

al. (2000, 2001) investigate the response of a mixed layer isopycnal ocean GCM to chlorophyll pigments in the Arabian Sea and the equatorial Pacific. In their experiments the ocean GCM is driven with an atmospheric forcing and possible ocean–atmosphere feedbacks are not included. A global ocean GCM is applied by Manizza et al. (2005) to look at the bio-optical feedbacks between phytoplankton, ocean dynamics and sea ice. Possible atmospheric responses are discussed in Shell et al. (2003). They first run an ocean GCM to obtain the biologically induced modifications of the sea surface temperature (SST) and then run a global atmospheric simulation using the modified SST. Again, possible ocean–atmosphere feedbacks are not included. A highly simplified coupled atmosphere–ocean model is applied by Marzeion et al. (2005) and Timmermann and Jin (2002) to study the influence of ocean biology on the tropical climate. Ocean turbidity through depth-dependent attenuation of solar radiation is also investigated in a bulk-type mixed layer model by Kara et al. (2004). Potential influences of phytoplankton in the Pacific on long-term climate variations are discussed by Miller et al. (2003).

In this paper, a fully coupled, state-of-the-art climate model is, for the first time, utilized to investigate the influence of marine phytoplankton on global climate and its variability. The climate model includes an ocean/sea ice GCM [Max Planck Institute Ocean Model (MPI-OM)] coupled online to an atmospheric GCM (ECHAM5) using the Ocean–Atmosphere–Sea Ice–Soil (OASIS) coupler. Both models are briefly described in section 2. With this system we are able to investigate the impacts on the SST, the resulting atmospheric changes, and the feedback to the ocean dynamics. After discussing the global patterns in section 3 we focus on regions of special interest in section 4. These regions include the equatorial Pacific and the Arabian Sea, as well as the temperate oceans. We also address temperature and precipitation changes over land. In section 5, we summarize the results and draw some conclusions as to the importance of the radiative attenuation effect of marine phytoplankton on the global climate.

2. Model description

a. Ocean general circulation model

The Max-Plank-Institute Ocean Model, MPI-OM, is a z-coordinate global general circulation model based on primitive equations for a hydrostatic Boussinesq fluid formulated with a free surface. Advection is computed with a second-order total variation diminishing (TVD) scheme (Sweby 1984). It includes parameterizations of subgrid-scale mixing processes like isopycnal diffusion of the thermohaline fields and eddy-induced tracer transport, following Gent et al. (1995), and a bottom boundary layer slope convection scheme. The dynamic and thermodynamic sea ice model with viscous–plastic rheology and snow follows Hibler (1979). The model uses an orthogonal curvilinear C grid with a formal resolution of 1.5°. In this setup, one pole is located over Greenland and the other over Antarctica. The horizontal resolution gradually varies between 15 km in the Arctic and about 184 km in the Tropics. It has 40 vertical levels with level thickness increasing with depth. Eight layers are within the upper 90 m and 20 are within the upper 600 m. The time step is 80 min. Bathymetry was created by interpolation of the Earth Topography Five Minute Grid (ETOPO5) dataset (National Geophysical Data Center 1988) to the model grid. For details on MPI-OM and the grid versions, see Marsland et al. (2003). A parameterization that accounts for the effect of ocean currents on surface wind stress (Jungclaus et al. 2006) is also included.

b. Biogeochemical model

The Hamburg Oceanic Carbon Cycle Model (HAMOCC5) simulates marine biology and biogeochemical tracers in the oceanic water column and the sediment. HAMOCC5 is coupled online to the circulation and diffusion of the MPI-OM ocean model, running with the same vertical and horizontal resolution and time step. Biogeochemical tracers are transported and mixed with the ocean advection and mixing schemes. The carbon chemistry is identical to the HAMOCC3 version of Maier-Reimer (1993). The ecosystem model is based on nutrients, phytoplankton, zooplankton, and detritus (NPZD type) as described by Six and Maier-Reimer (1996). In addition new elements such as nitrogen, dissolved iron, and dust are accounted for and new processes like denitrification and N fixation, formation of calcium carbonate and opaline shells, dimethyl sulfide production, dissolved iron uptake and release by biogenic particles, and dust deposition and sinking are implemented. The dust fields for the experiments in this paper are taken from a model simulation by Timmreck and Schulz (2004). The model contains a sediment module following Heinze et al. (2003), including opal, silt, organic carbon, and calcium carbonate. A complete technical documentation (Maier-Reimer et al. 2005) of HAMOCC5 is available online.

c. Atmospheric general circulation model

The atmospheric general circulation model ECHAM5 (Roeckner et al. 2003) has evolved from the model of

the European Centre for Medium-Range Weather Forecasts (ECMWF). ECHAM5 solves prognostic equations for vorticity, divergence, surface pressure, and temperature expressed in terms of spherical harmonics with a triangular truncation. Water vapor, cloud liquid water, cloud ice, and trace components are transported with a flux form semi-Lagrangian transport scheme (Lin and Rood 1996) on a Gaussian grid. The solar radiation scheme (Fouquart and Bonnel 1980) has four spectral bands, one for the visible and ultraviolet, and three for the near-infrared. The horizontal resolution is T63 in spectral space, which corresponds to approximately 1.75° on a Gaussian grid.

d. Atmosphere ocean coupling

The atmosphere and ocean models run on different grids and with different time steps. They are coupled with the OASIS coupler (Valcke et al. 2003) with a coupling time step of one day. The ocean passes the SST, sea ice concentration and thickness, snow depth, and the surface velocities to the atmosphere through OASIS. The atmosphere uses these boundary conditions for one coupling step and then transfers the surface forcing fields through OASIS back to the ocean model. Required surface forcing fields are heat, freshwater and momentum fluxes, and the 10-m wind speed.

e. Model initialization and experiment setup

Two experiments are described in this study: a control run with constant shortwave attenuation in the upper ocean ("fixed ocean") and an experiment with interactive marine biology ("green ocean"). The control run (fixed ocean) is identical to the experiment with wind stress correction (WSC) as described by Jungclaus et al. (2006). We choose the Jungclaus et al. (2006) experiment as our control experiment because it is well tested and gives very good results, especially within the equatorial Pacific region. The green ocean is started from the same initial conditions as the fixed ocean experiment and is integrated for 125 years.

There are different requirements for comparing fully coupled experiments than for comparing forced simulations. In a forced simulation one can compare a clear water case to an ocean with light absorption by chlorophyll: Whereas in a fully coupled climate system such a change would lead to a different mean state and the nonlinear feedbacks within the system would make the two experiments very difficult to compare to each other. Also it is not easily possible to take, for example, a chlorophyll climatology from from the Sea-Viewing Wide Field-of-View Sensor (SeaWiFS) satellite. Even so, such a climatology is more realistic than our simulated chlorophyll distribution; it does not fit into the "fully coupled world" because the simulation cannot possibly be 100% identical to the "real world" in time and space. Therefore, in this experiment, the interactive biology is used for consistency. We are not able to separate the possible effects of an interactive versus a climatological biology.

In the fixed ocean experiment, solar radiation is absorbed with a constant e-folding depth of 11 m ($1/e$ of the light is left after 11-m depth). In the green ocean the incoming radiation is equally split into two wavelength bands. The first half consists of ultraviolet (UV) and infrared (IR) light and is fully absorbed within the first layer of the ocean model. The remaining half (I_0) is absorbed as a function of depth (z) according to the following equation, with a term for pure water and a term that is linear to the phytoplankton concentration:

$$I_z = I_0 e^{k_w z} e^{k_{\mathrm{chl}} z}. \quad (1)$$

Analogously to Moore et al. (2002), the attenuation coefficient for pure water is chosen to be $k_w = 0.04\ \mathrm{m}^{-1}$ and the coefficient linear to the phytoplankton concentration is computed as $k_{\mathrm{chl}} = 0.03\ [\mathrm{Chl}]\ \mathrm{m}^{-1}$, with the chlorophyll concentration given in mg Chl L^{-1}. Chlorophyll is computed from phytoplankton with a fixed chlorophyll : carbon ratio of 1:80. There are more complex and more complete ways to calculate chlorophyll concentrations (Cloern et al. 1995) and to describe the radiation distribution (Morel and Maritorena 2001). However, the prerequisite for this experiment is that the two simulations of the climate system are comparable. Therefore, we intentionally keep the description as simple and easy to control as possible to ensure that the average penetration depth of the green ocean is not too different compared to the penetration depth of the fixed ocean experiment.

3. Results

a. Global oceanic patterns

The penetration depth reflects the average distribution of chlorophyll. Figure 1 shows seasonal averages of chlorophyll distribution for the boreal summer and boreal winter from the SeaWiFS satellite[1] and from the model. The chlorophyll concentration of the model is determined from the modeled phytoplankton biomass

[1] Data are provided by the SeaWiFS Project (Code 970.2) and the Distributed Active Archive Center (Code 902) at the Goddard Space Flight Center, Greenbelt, MD 20771. These activities are sponsored by the NASA Mission to Planet Earth Program.

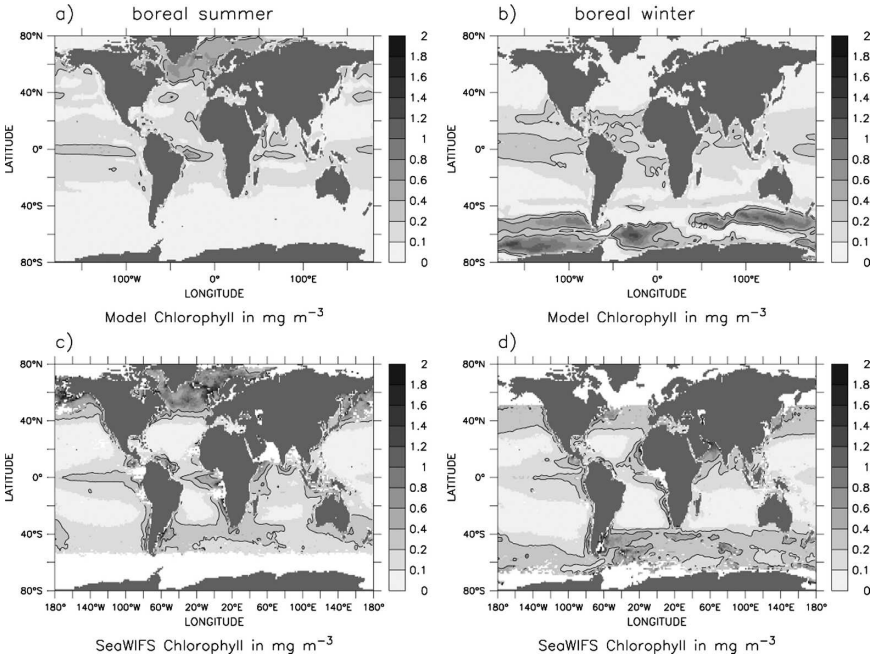

FIG. 1. Seasonal averages of chlorophyll distribution for the boreal summer and the boreal winter. Shown are (top) simulation results from the model and (bottom) data from the SeaWiFS satellite.

multiplied by a fixed chlorophyll : carbon ratio of 1:80. The model captures the global pattern and the dynamics of the seasonal cycle. High chlorophyll concentrations in coastal areas cannot be reproduced by the model because shelf processes and riverine input of nutrients are not captured. Although there is evidence that SeaWiFS overestimates the winter chlorophyll distribution (Conkright and Gregg 2003), the model underestimates the chlorophyll concentrations north and south of 40° during the respective winters. For this experiment this does not pose a problem because solar radiation is weak and the mixed layer is deep in those areas during these times of the year. The boreal summer bloom is slightly underestimated by the model while in the Southern Ocean it is overestimated. This leads to a larger-than-observed seasonal cycle in the south. The possible error is not large because the sensitivity of this experiment to an over- or underestimation of a phytoplankton bloom with high chlorophyll concentrations is limited. This is because the thickness of the upper box (12 m) is setting an upper limit to the total sensitivity of the model to light absorption by chlorophyll. The radiation absorbed in the uppermost box cannot exceed the total radiation entering the ocean no matter what the concentrations are. Also captured is the phytoplankton bloom due to upwelling during the summer monsoon in the Arabian Sea.

Averages of the resulting *e*-folding penetration depth ($k_w + k_{\text{chl}}$) are shown in Fig. 2. In the subtropical gyres the penetration depth is nearly identical to that of clear water year round (25 m in our model), but in the upwelling regions at the equator it is always lower. In high-latitude regions, penetration depth shows a strong seasonal cycle with low penetration in their respective summers and high penetration in their respective winters.

Heat flux in the upper ocean, modulated by phytoplankton, affects not only the SST but also the mixed layer depth (MLD). When more of the solar radiation is absorbed at the surface, surface waters warm up, the water column becomes more stable, and the MLD shoals. Less cold, subsurface water is mixed to the surface and the surface water becomes even warmer. The converse is also true: When more solar radiation is able to penetrate into deeper layers, surface waters stay colder and the lower layers heat up more. This leads to a destabilization of the water column and a deeper MLD. More cold, subsurface water is mixed to the surface and the surface water becomes even colder. Therefore the changes in the MLD act as an amplification of the effect of phytoplankton on SSTs that is larger than the direct warming effect. MLD differences in the temperate oceans are mostly around ±5 m. The MLD of the green ocean is shallower in summer and deeper in winter compared to the fixed ocean. On annual average the MLDs are deeper in the subtropical gyres and shal-

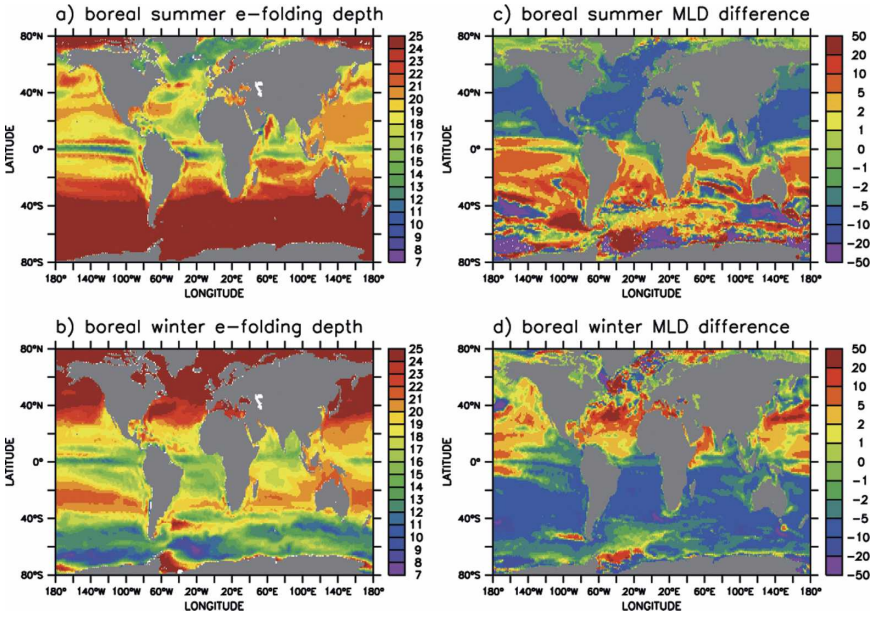

FIG. 2. (left) The 90-yr average of the green ocean *e*-folding depth ($k_w + k_{chl}$) in meters. (a) Average *e*-folding depth during northern summer (June–August) and (b) during northern winter (December–February). (right) The 90-yr average of the mixed layer depth difference between the green ocean and the fixed ocean experiment in meters. (c) Average MLD difference during northern summer (June–August) and (d) during northern winter (December–February).

lower in the upwelling regions at the equator and along parts of the western coastline. Naturally the differences are larger in winter at high latitudes where the MLDs are deeper, but the fractional change is not larger than elsewhere. In addition, variable attenuation does not play a major role there in winter because solar radiation is weak and much of the changes can be explained by changes in the wind fields and in the sea ice cover. Shifts in the wind field patterns also cause the considerable differences in the "Roaring Forties" in the Southern Hemisphere during austral winter (not shown).

Ocean–atmosphere interactions are determined by the SST. However, redistributing heat in the surface ocean not only changes the SST, but also the temperature in the subsurface layers and the stability of the water column. A deepening of the ML also mixes warm surface waters into deeper layers. Temperature differences between the green ocean and the fixed ocean experiment at the surface and down to 280 m are shown in Fig. 3. In contrast to the seasonal cycle at the surface, these large-scale temperature change take decades to develop in the model. Therefore, Fig. 3 shows an average over the last 40 years of the simulation. Changes in SST between 40°N and 40°S are small but, because of deeper mixing and transport processes, changes of up to 1°C in some areas reach as deep as 200 to 300 m. The strongest warming in those deeper layers occurs in the Indian Ocean and the western Pacific. Warmer waters from the subtropics are transported equatorward. Between 20°N and 20°S the thermocline deepens and becomes steeper toward the subtropics (the deepening of the 20° isotherm depth is shown in contour lines in Fig. 3). Temperature differences between 20°N and 20°S are at a maximum around 100 m. Just underneath the surface at about 50-m depth, the warming concentrates at the equatorial upwelling regions and along the western coastline of Africa and South America. North and south of 20° the water is colder. Through mixing and upwelling the subsurface temperatures at the equator influence the temperatures near the surface. In this model, the warming of the "cold tongue" in the equatorial Pacific is to a large part due to the deepening of the thermocline.

b. Global atmospheric patterns

The zonal mean temperature differences (green minus fixed ocean) in Fig. 4 show that the influence of the SST changes extend through the troposphere. The dominant pattern is the amplification of the seasonal cycle. During the northern summer we find a warming north of 30°N and a cooling in the Southern Hemisphere, strongest around 60°S. During the northern winter this pattern partly reverses. Owing to a retreat in

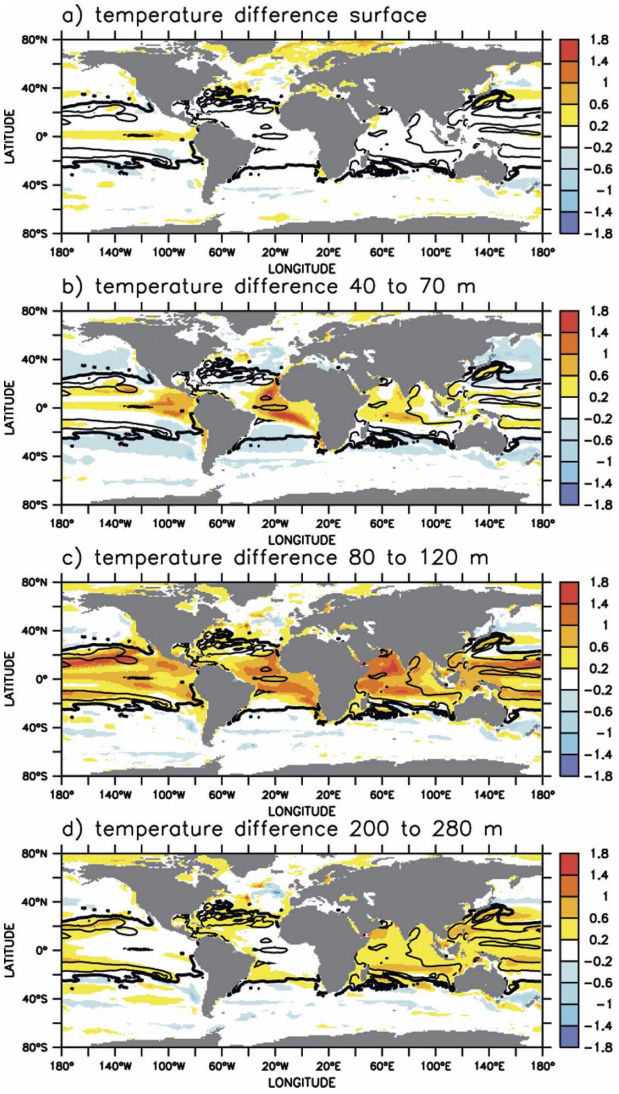

FIG. 3. Annual average over the last 40 years of temperature differences between the green ocean and the fixed ocean experiment in degrees Celsius: (a) the SST and (b) the average for the water column between 40 to 70 m, (c) 80 to 120 m, and (d) 200 to 280 m. Contour lines denote the deepening of the 20° isotherm depth between the two experiments in 10-m intervals.

sea ice, the high latitudes are warmer in their respective winters. Air temperatures over the equatorial regions are warmer year round. SSTs across the tropical Pacific contribute significantly to the observed patterns of tropical rainfall. In the green ocean experiment, rainfall is higher over the western tropical Pacific and slightly lower in the eastern equatorial Pacific. North and south of the equator there is a shift in the rainfall patterns. The wind systems across the tropical Pacific are associated with the equatorial patterns of SST and rainfall. In the green ocean experiment, the Hadley cells become stronger and, in contrast to Shell et al. (2003), we also find a minor increase of the Walker circulation.

c. *Seasonal changes*

From the subtropics to high latitudes we generally see an amplification of the seasonal cycle and the warming of the sea surface in spring starts about two weeks earlier. Temperature changes also occur over land and are often larger than over water. Figure 5 shows the temperature differences between the green ocean and the fixed ocean for four seasons (northern spring to winter) and lines marking the 99% significance level. During northern spring and summer, most of the warming occurs north of the subtropical gyres and extends well over land. Between 20° and 60°N there is a cooling in winter that is even stronger over land. Along with the amplification we find a shift of the seasonal cycle by about 2 weeks. To illustrate the shift, Fig. 6 shows two time series of SSTs from 40°N in the Pacific and the Atlantic and 40°S in the Pacific. In the Southern Hemisphere the shift of the seasonal cycle is also on the order of two weeks, but the SST differences are smaller. The earlier start of the spring warming is directly caused by the influence of the phytoplankton spring bloom on the upper surface heating and the MLD. Comparison with SST data from the National Centers for Environmental Prediction–National Center for Atmospheric Research (NCEP–NCAR) reanalysis (Kalnay et al. 1996) shows that the shift makes the simulation of the seasonal cycles more realistic. This is an indication that phytoplankton has an influence of similar magnitude on the seasonal cycle in the real world.

Sea ice in the Arctic and Antarctic is generally lower in the green ocean experiment, with stronger retreat in the north. This is associated with a warming of the SST in high latitudes of about 0.4°C north of 60°N and 0.1°C south of 60°S, on the annual average. While summer SSTs are warmer in the Labrador Sea, along the coast of Greenland, and in the Barents Sea, temperatures over the Arctic are higher in autumn and winter. This influences the land temperatures over Siberia and Alaska in the autumn.

The atmosphere is influenced by the ocean through latent and sensible heat fluxes and, to a minor degree, by the outgoing longwave radiation (all of which are related to the SST). Sensible heat flux from the surface to the atmosphere by conduction and convection directly affects the temperature in the lower atmosphere. Latent heat flux transfers energy when liquid water is converted into vapor. This vapor is transported by atmospheric circulation vertically and horizontally and is

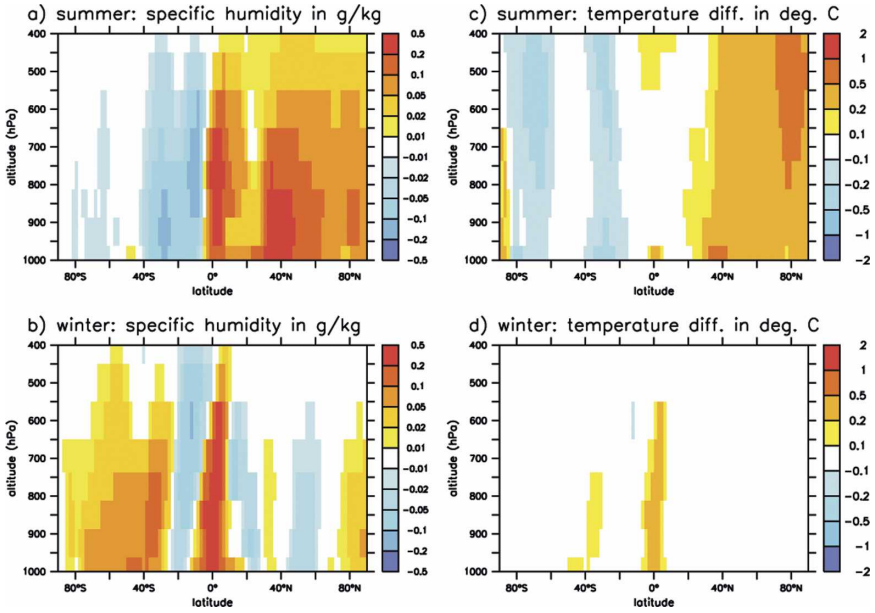

FIG. 4. Zonal average of temperature and specific humidity over the Pacific. Shown are differences between the green ocean and the fixed ocean experiment from the ground up to 400 hP: averaged from (a), (c) June to August and (b), (d) from December to February.

eventually condensed as rain or deposited as snow, releasing the latent heat energy stored within. Some of the outgoing longwave radiation is absorbed in the atmosphere while the other part escapes to space. Most of the feedback is provided in the form of changes in wind stress, shortwave radiation, and precipitation. Heat flux and atmospheric feedbacks for the regions used in Fig. 6 can be seen in Fig. 7. Precipitation (results not shown) generally increases between 10°N to 10°S over the Tropics and decreases between 30° to 10° over the subtropics. Precipitation also increases by 3 mm day^{-1} along the coast of India when winds blow over the Arabian Sea during the summer monsoon from July to September. Elsewhere the changes in precipitation are small. Another feedback is due to the shortwave radiation incident on the ocean. On average, shortwave radiation is up to 4% higher over the eastern equatorial Pacific and about 4% lower elsewhere in the Tropics.

The strong warming north of 30°N during boreal summer is not replicated in the Southern Hemisphere during the austral summer (Fig. 5). The reason for this asymmetry is that the summer warming in the north is amplified by a reduction in cloud cover, resulting in an increase of shortwave radiation by about 10% (Fig. 7). The reduction in cloud cover cannot be explained with local feedbacks, but with atmospheric teleconnections from the SST anomaly in the equatorial Pacific. Figure 5 shows that the SST difference there is high in spring (March, April, and May) and low during the rest of the year. The teleconnection is based on a strengthening of the Hadley circulation with higher precipitation over the equator and anomalous drying and warming in the subtropical subsidence regions. This "atmospheric bridge" connects the equator and the extratropics with a time lag of about 2–3 months (Alexander et al. 2002) and explains the amplification of the marine biota–induced warming in June, July, and August. The anomalous warming north of 30°N in the Pacific and the Atlantic during the boreal summer abruptly ends at the beginning of autumn (Fig. 7) when the wind stress increases. Although the cloud cover north of 30°S over the Southern Hemisphere is reduced at the same time in the green ocean, this does not result in warmer surface temperatures for two reasons: First, there is less solar radiation during the austral winter and, second, owing to the enhanced seasonal cycle the surface temperatures are already lower in the Southern Hemisphere and the increase in shortwave radiation only moderates the cooling.

d. Regions of special interest

1) EQUATORIAL PACIFIC

The region of upwelling along the equatorial Pacific is called the cold tongue. In most state-of-the-art ocean GCMs the simulated cold tongue is colder than observed; this phenomenon is called the "cold bias." In

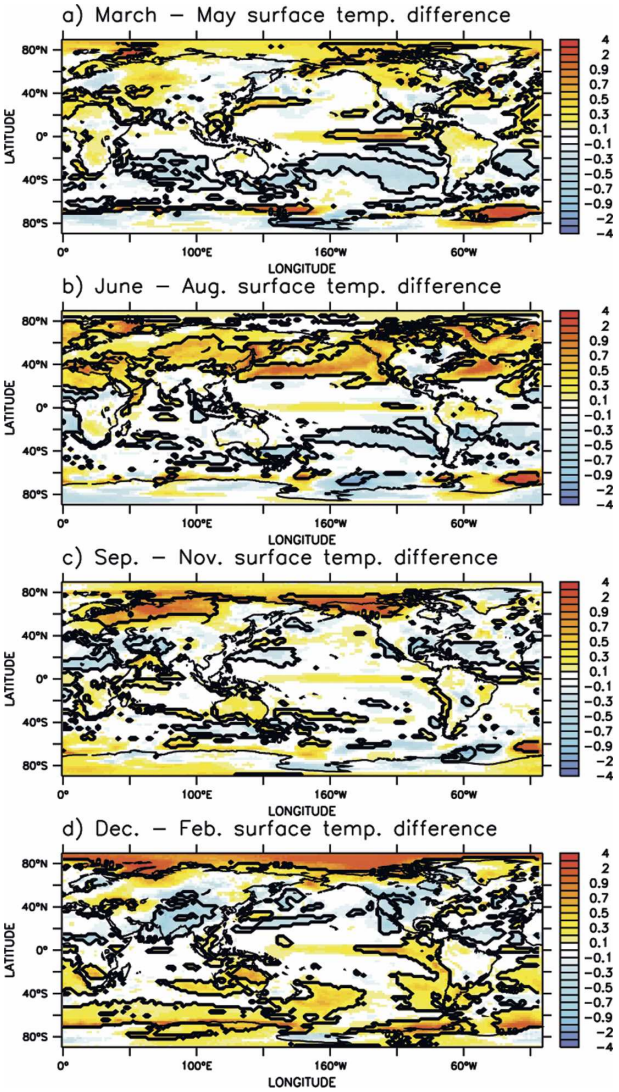

FIG. 5. Seasonal averages of the last 60 years of 2-m surface temperature differences between the green ocean and the fixed ocean experiment in degrees Celsius. The contour lines mark the 99% significance level. The average for (a) March–May, (b) June–August, (c) September–August, and (d) November–February.

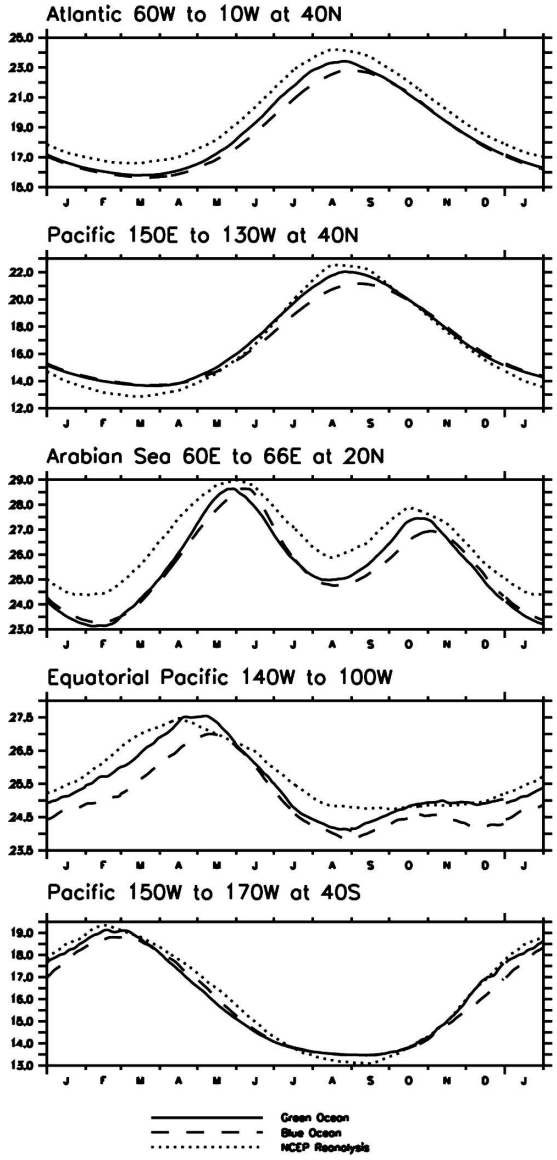

FIG. 6. Seasonal SST cycle of the green ocean and the fixed ocean experiment in the North Pacific, North Atlantic, Arabian Sea, equatorial Pacific, and South Pacific. Shown are 50-yr averages of daily values. Also shown for comparison are climatological averages from the NCEP–NCAR reanalysis.

coupled ocean–atmosphere models the offset is usually larger than in forced simulations because of coupled feedbacks. In addition, a cold anomaly in the eastern equatorial Pacific leads to an increase of the trade winds and amplifies the anomaly. This is known as the Bjerknes feedback. Taking into account the effect that surface currents have on wind shear has improved the model significantly (Jungclaus et al. 2006). However, the model still shows a cold bias of more than 1°C, mostly during the upwelling season from July to September. In the green ocean this bias improves by over 0.5°C on average (Fig. 3a). Figure 6 shows the seasonal cycle of SST differences in the equatorial Pacific. Most importantly, the spring warming begins earlier and the peak has shifted by 2–3 weeks from May to April with the SST in April being up to 1.2°C warmer. The direct comparison with SSTs from the NCEP–NCAR reanalysis (Kalnay et al. 1996) shows that the shift of the spring warming and the increase in temperature is an improvement toward a more realistic representation of the seasonal cycle in the equatorial Pacific. During the upwelling season the green ocean is only slightly warmer

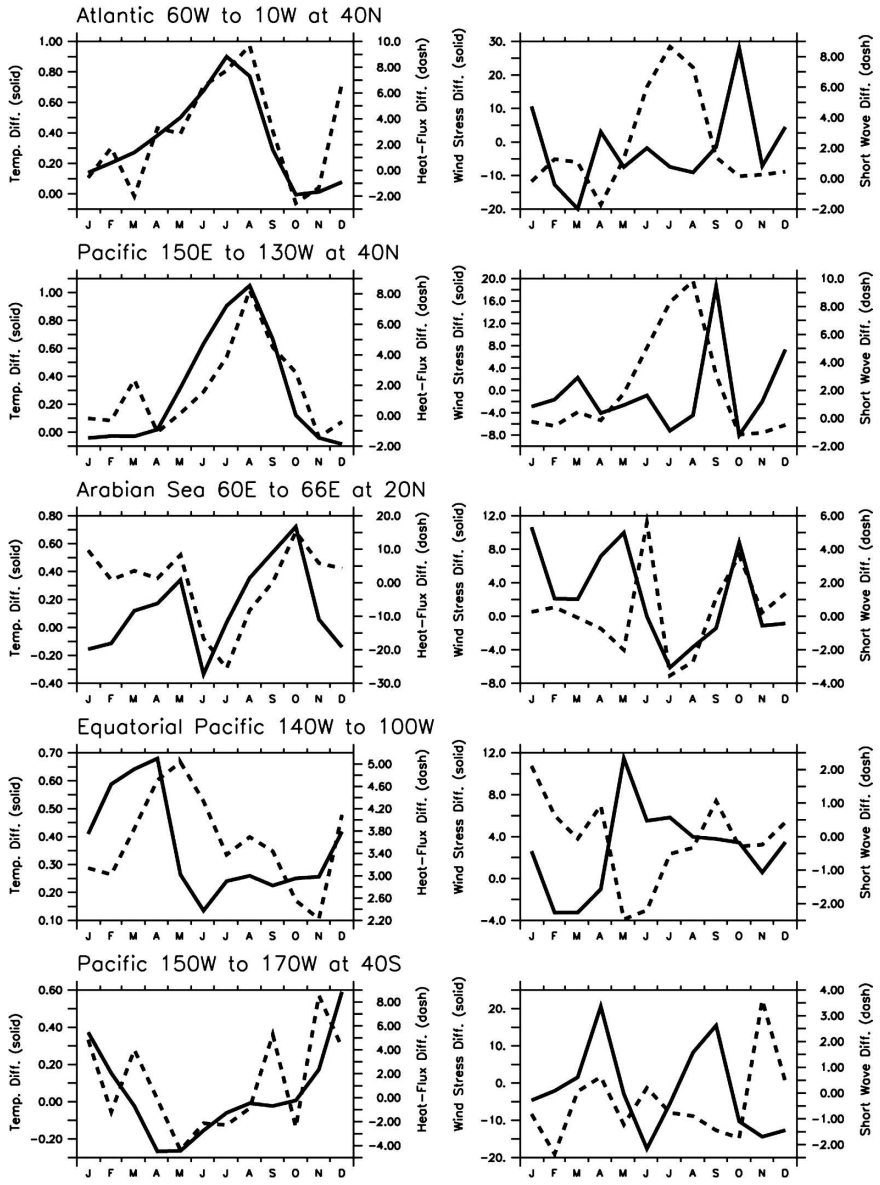

FIG. 7. (left) Solid lines are surface temperature differences in degrees Celsius. Dotted lines are the changes in the sensible and latent heat flux (ocean to atmosphere) in W m^{-2}. (right) Feedbacks from the atmosphere to the ocean. Solid lines are percentage of wind stress differences, and dotted lines are shortwave radiation in W m^{-2}. Shown are 90-yr averages of the seasonal cycle from the green ocean and the fixed ocean experiment in the North Pacific, North Atlantic, Arabian Sea, equatorial Pacific, and South Pacific.

than the fixed ocean and both experiments are up to 1°C colder than the NCEP–NCAR reanalysis SST.

In contrast to our results, Murtugudde et al. (2002) find that the effects of penetrative radiation are largest during the upwelling season. Their finding is in agreement with a sensitivity study (results not shown) conducted with a HAMOCC/MPI-OM ocean and biogeochemical model identical to the version used for this study, but forced with surface fluxes from the NCEP–NCAR reanalysis (Kalnay et al. 1996). This is surprising, as the mechanisms that cause the warming in the equatorial Pacific are the same in both the stand-alone ocean and the coupled ocean–atmosphere model. Most of the warming is caused by deepening of the thermocline (Fig. 3). In addition, nutrients upwelled from below during the cold phases cause an increase in the phytoplankton biomass, which again traps the heat of the solar radiation absorbed near the surface. It is the

atmospheric coupling that reverses the seasonal pattern. In spring, SSTs are warmer at the equator and colder in the subtropics. This causes a strengthening of the trade winds (Fig. 7), which leads to stronger upwelling and almost completely counteracts the warming mechanisms in the following month.

2) Arabian Sea

Accurate simulation of SSTs in the Arabian Sea is important because it influences the monsoon system over the region. The seasonal cycle of the SST in the Arabian Sea has two maxima during the intermonsoon periods and minima during the southwest summer monsoon (June–September) and during the northeast winter monsoon (December–March). Satellite observations from SeaWiFS show a chlorophyll peak during the onset of spring (February and March) and in the newly upwelled waters from July to September. The model captures the low chlorophyll concentrations observed by SeaWiFS from November to January and the rise at 20°N in spring, but it underestimates the boreal summer bloom (not shown). However, we find the largest differences between the fixed and the green ocean experiments in autumn. Surface temperatures in the west are over 1°C warmer and the warming stretches to the east at 20°N. In addition, the warming after the summer monsoon starts almost one month earlier and the peak also shifts by 2–3 weeks. During the summer monsoon from July to September, when the winds blow over the Arabian Sea, precipitation along the coast of India increases by about 3 mm day^{-1}.

One would expect a large influence from the phytoplankton during the spring bloom in February and March, but we find only a shift of the peak by 1–2 weeks and no additional warming. However, Fig. 6 indicates that both the warming and the shift lead to a representation of the seasonal cycle that is more similar to the SST from the NCEP–NCAR reanalysis (Kalnay et al. 1996). Figure 7 shows that the wind stress during both monsoon seasons has also increased in the green ocean experiment. In this model, SST anomalies in autumn mostly result from the deeper thermocline in the green ocean experiment. The shifts in the seasonal cycle in spring and autumn cannot be explained by local feedbacks, but only by the large-scale shift in the seasonal cycle in the Northern and Southern Hemispheres.

Our results are again quite different to the studies without atmospheric feedbacks by Murtugudde et al. (2002) and Nakamoto et al. (2000). They both find the maximum warming in March and April, a slight cooling from July to August, and a minor warming from October through January.

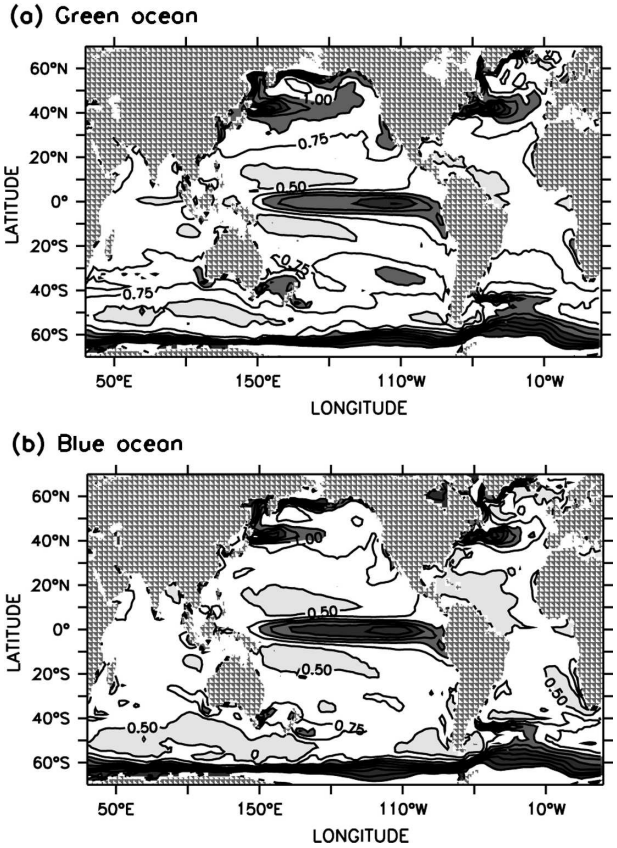

FIG. 8. Standard deviation of SST anomalies from years 25 to 115 of (a) the biologically active (green ocean) and (b) biologically inactive (fixed ocean) simulations. The contour interval is 0.5°C, with values less (larger) than 0.5°C (1.0°C) shaded light (dark).

e. *Tropical Pacific interannual variability*

In this section the impact of biology on the interannual variability of the tropical Pacific is described. For this purpose only years 26 to 115 of both simulations are considered. The period is limited by the length of the green ocean simulation, and the first 25 years of the simulations are considered as part of the model spinup.

One impact of biology in the model is a reduction in variability. In the central eastern Pacific the standard deviation of the SST drops by around 15%, from 1.75° to 1.5°C (Fig. 8). The observed value is somewhere between 1° and 1.5°C, depending on both the period considered and the dataset used. The structure of the variability is also reminiscent of the observations, except that it extends too far into the warm pool. Variability in the extratropics, under the storm track zones, is overestimated; the causes for this are being investigated. Compared to the control simulation, the global

structure of the interannual variability remains quite similar.

It has been suggested (Timmermann and Jin 2002) that biological processes may contribute to the skewness of ENSO variability. In our simulation there are some hints that negative ENSO events are slightly more damped than the positive ones: in the biologically active simulation Niño-3 (5°S–5°N, 150°−90°W) averaged SST anomalies vary between −3° and 3.5°C (Fig. 9b), whereas in the biologically inactive simulation Niño-3 SST anomalies vary from −3.5° to 3.5°C (Fig. 9c). Observed variability over the last 100 years [Rayner et al. 2003: Hadley Centre Sea Ice and SST dataset (HadISST)] varies from around −2°C to almost 3.5°C (Fig. 9a). The frequency of strong positive events (greater than, say, 3°C) is also slightly reduced in the biologically active simulation and is more consistent with the observations. The histogram of Niño-3 SSTs from the green ocean simulation compares more favorably to the observed one than that of the simulation without biology (Fig. 10). Thus, biological processes may positively affect the skewness of ENSO in our simulation; however, these changes may well not be statistically significant given the brevity of our simulation.

The inclusion of biological processes also brings improvements to the seasonal variations in ENSO variability. The observed variations show the strongest

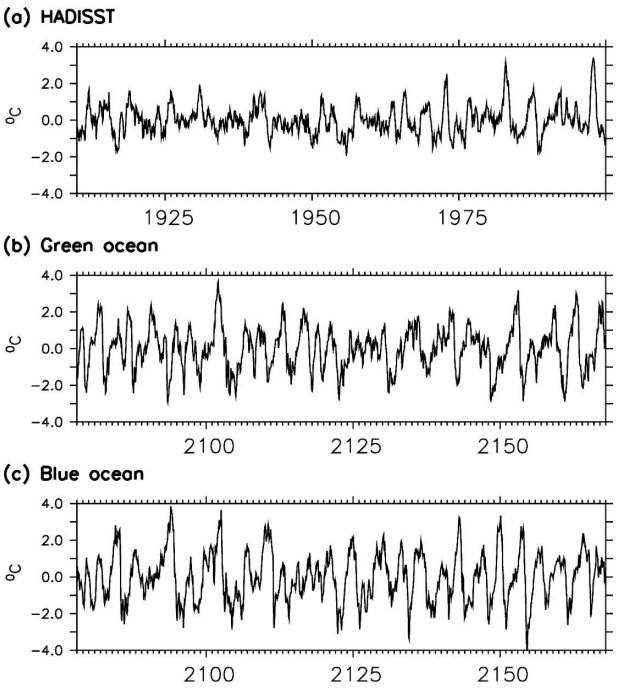

FIG. 9. Niño-3-averaged SST anomalies from (a) observations (HadISST) between 1910 and 1999 and years 25 to 125 of (b) the biologically active and (c) biologically inactive simulations.

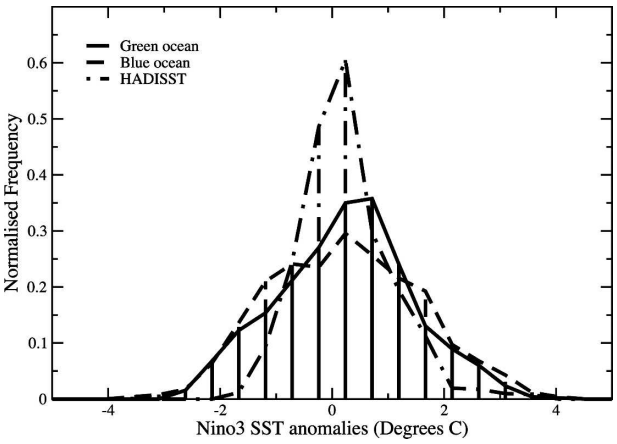

FIG. 10. Histogram of the Niño-3-averaged SST anomalies shown in Fig. 9.

variability in December and the weakest variability in April (Fig. 11). Both biologically active and inactive simulations have significantly stronger variability than the observations in all calendar months (Fig. 11), although the biology run is always weaker than the control run. The differences are most pronounced in April, with the observed minimum in variability better represented in the green ocean. This is an indication that the termination of ENSO events is better represented in the biological simulation. The unrealistic second peak in variability that occurs in late boreal summer in both simulations is also less pronounced when biota are included. This second peak is mainly the result of the poor simulation of negative anomalies.

The inclusion of biological processes also improves the simulation in terms of the periodicity of interannual variability. The observed spectrum of Niño-3 SST

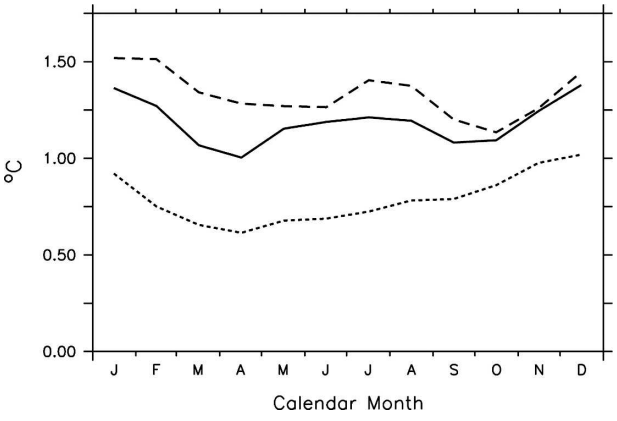

FIG. 11. Standard deviation of Niño-3-averaged SST anomalies as a function of calendar month for HadISST observations (1910–99, dotted) and years 25 to 125 of the green ocean (solid) and fixed ocean (dashed) simulations.

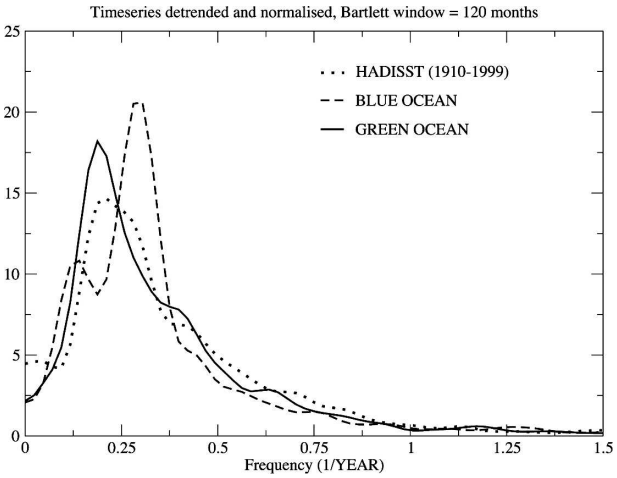

FIG. 12. Power spectra of Niño-3-averaged SST anomalies from HadISST observations (1910–99) and years 25 to 125 of the green ocean and fixed ocean simulations.

anomalies calculated for the time span from 1910 to 1999 shows a broad peak between 3 and 5 yr, and a second weaker bump around 2.5 yr (Fig. 12). Only 90 years of observations are considered here to be consistent with the length of the simulations. The biologically inactive simulation shows a sharp spectral peak at around 3.5 yr and a second weaker peak at 8 yr (Fig. 12). When a longer period of the simulation is considered this second peak weakens, and the main peak shifts to around 4 yr. The inclusion of biological processes causes the spectral peak to broaden, and the dominant period to shift to 5 yr, in better agreement with the observations (Fig. 12). A weak bump at around 2.5 yr is also simulated but, given the brevity of the time series, it may not be a significant feature of the spectrum.

The propagation characteristics, and the spatial structure of SST anomalies simulated in the green ocean run are quite similar to that of the biologically inactive fixed ocean simulation, and are only briefly described here (see Jungclaus et al. 2006). Simulated SST variability is weak west of 140°W and strongest in the central and eastern Pacific, where anomalies range between ±4°C. These aspects compare favorably with observed SST variability, which is weak west of the date line; in the central Pacific anomalies range between ±1° and 2°C, and in the east they range between −2° and 4°C. The westward extension of the anomalies and their intensity in the central Pacific are overestimated (not shown). However, similar to the observations, SST anomalies tend to develop at almost the same time in the east and central Pacific. Also reminiscent of the observations, individual events appear to propagate sometimes weakly eastward or westward. The meridional extent of the ENSO-related SST anomalies is very similar in both simulations, and also similar to the observations (Jungclaus et al. 2006).

In summary, the inclusion of biological processes reduces the strength of interannual SST variability by about 10%–15%, improves the skewness and phase locking to the annual cycle, increases the dominant ENSO period to around 5 yr, and broadens the ENSO spectral peak. Changes in ENSO properties are caused by changes in the ENSO feedbacks, which in turn may result directly from changes in model physics or indirectly from changes in the mean state.

As discussed above, the inclusion of biological processes results in a warming of 0.5°C in the eastern Pacific. The warming is, however, not primarily due to a shoaling of the mixed layer since close to the equator the mixed layer depth shoals by no more than 3 m. The warming appears primarily due to a deepening of the thermocline from 20°S to 20°N (about 10 m on average), which at the equator results in warmer water being upwelled. The warming effect is, however, somewhat compensated for by a strengthening of the overturning of the subtropical cells, including equatorial upwelling, of about 10%. The changes in the subtropical cells and the deepening of the thermocline are driven by changes in the tropical wind stress curl, and not by changes directly at the equator where the mean zonal winds are hardly affected. The Bjerknes feedback is apparently not excited in our model since the induced SST anomalies are located too far east of the convection.

Despite the deepening of the thermocline, the thermocline–SST feedback in the eastern Pacific (150°E–90°W) was insignificantly changed. The damping effect of the atmosphere there is also hardly changed. In contrast, the sensitivity of the atmosphere to SST anomalies is increased back to levels close to those seen before the introduction of the wind shear correction (Jungclaus et al. 2006). This change would, however, argue for an increase in ENSO variability, in contrast to the decrease simulated.

The interaction between biological processes and ENSO is investigated to see if it could explain the simulated decrease in ENSO variability. In our simulation, the relationship between biological activity and upwelling was highly nonlinear: the two are only related below a certain upwelling threshold. Below this threshold increases (decreases) in upwelling result in increases (decreases) in phytoplankton concentration and, hence, to a reduction (increase) in the optical attenuation depth. Above this threshold biological activity is controlled by other factors. Furthermore, upwelling and ENSO activity are strongly related only in

the central Pacific in our model. Thus only in the central Pacific, and only during warm events, is there any coherent variability in phytoplankton concentration: a decrease in phytoplankton concentration and an increase in the optical penetration depth is seen. This may support a reduction in the strength of warm events, due to the direct effect of deeper penetration of solar radiation, but does not argue for any change in cold events. Our model simulates no coherent changes in mixed layer (also known as the indirect effect).

Analysis of the relevant ENSO feedbacks would thus suggest that the changes in the simulated ENSO properties are due to changes in the mean state. Indeed the theoretical work of Federov and Philander (2001) predicts that deepening of the thermocline by about 10 m would result in a lengthening of the ENSO period on the order of the simulated change. In their work, a deepening of the thermocline results in a shift toward a more "thermocline mode." From our analysis it is, however, hard to confirm that this is indeed the case. A shift toward such a regime should also result in changes in ENSO amplitude, but such a relationship seems not to have been discussed in the literature.

Our results are in contrast to those of Marzeion et al. (2005). In their hybrid coupled modeling study, the inclusion of biological processes results in a decrease in the strength of the annual cycle, an increase in ENSO activity, and an increase in the dominant ENSO period (from 2 to 3 yr). In their case, the strengthening of ENSO variability is due to weakening of the annual cycle. Our results are consistent with theirs in so far as we get a lengthening of the ENSO period and that they also show the importance of coupled interactions. However, our results differ from theirs in that we get very little change in the strength of the annual cycle, and our ENSO variability decreases in strength. Unlike them, in our model the Bjerknes feedback is not strongly excited, and the changes in ENSO properties are largely driven by changes in the off-equatorial winds. In our model the indirect effect on mixed layer depth is also not active.

4. Conclusions

We investigate the influence of phytoplankton on the seasonal cycle and the mean global climate in a fully coupled climate model. We primarily do this by analyzing the differences between a "green ocean" with phytoplankton and a "fixed ocean" control experiment without biology. One has therefore always to keep in mind that the way radiation is treated in the control experiment is as important for the difference between the two experiments as the effect of phytoplankton on the radiation. In this study, we use a fixed attenuation depth of 11 m in the fixed ocean control run and a green ocean setup where half of the radiation is absorbed in the first layer and the other half is attenuated with an attenuation depth that varies between 0 and 25 m, dependent on the presence of biota. With these settings, the average attenuation depth in the green ocean is about equal to the fixed attenuation depth in the fixed ocean, and the mean states of both systems are similar. This is a necessary prerequisite, as a fully coupled climate system has nonlinear feedbacks that would make two experiments with a different mean state very difficult to compare to each other.

Previous studies are all based on forced simulations, except those that use a simplified coupled system (Timmermann and Jin 2002; Marzeion et al. 2005). They therefore do not have such constraints and mostly use a "clear water" assumption (23-m attenuation depth) in their control experiments. This is an important factor to keep in mind when we compare our results with earlier studies. Murtugudde et al. (2002) refer to a control run that uses an attenuation depth of 17 m. They report that the warming of the water column below the mixed layer leads to a warming of SSTs in the equatorial Pacific cold tongue region of up to 1°C. This is in agreement with our findings. We find an even larger warm anomaly in the equatorial Pacific in the same model when we force it with surface fluxes from the NCEP–NCAR reanalysis (Kalnay et al. 1996; data not shown). Similar to Murtugudde et al. (2002) we also see a warming in the upwelling regions of the Arabian Sea.

In contrast, Nakamoto et al. (2001) and Manizza et al. (2005) compare the impact of phytoplankton to a control run with an attenuation depth of 23 m and both find a cooling in the Tropics. What appears to be in contradiction is actually consistent. Most of the warming in the Tropics is caused by a deepening of the thermocline, due to a deeper attenuation depth in the subtropics. With a clear water assumption in the control experiment, biota reduce the attenuation depth almost everywhere and the thermocline becomes more shallow, which results in a cooling along the equator. In addition, the impact of phytoplankton on SST and MLD is substantially different in different types of ocean GCMs. Kara et al. (2004) use a control run attenuation depth of 17 m in a bulk-type mixed layer model and only find minor impact of phytoplankton on the SST in the equatorial Pacific. Despite such differences, the direct influence of marine biology in our ocean model is similar to the results from previous studies. Like Manizza et al. (2005), we find that the seasonal cycle in the Northern and Southern Hemisphere is amplified and there is less sea ice in the high latitudes.

In addition to the amplification, we find a shift of the seasonal cycle by about two weeks. The earlier start of the spring warming is directly caused by the influence of the phytoplankton spring bloom on the upper surface heating and the MLD. The comparison with SST data from the NCEP–NCAR reanalysis shows that the shift makes the simulation of the seasonal cycles more realistic. This is an indication that the phytoplankton in the real world could have an influence on the seasonal cycle. The shift and the warming are more pronounced in the Northern Hemisphere. In the Southern Hemisphere the seasonal cycle is also shifted by about two weeks, but the SST differences are smaller. We attribute some of the additional warming north of 30°N to an atmospheric teleconnection from the Tropics. SST differences between the fixed and the green ocean in the equatorial Pacific are not uniform over the year. The warm anomaly is high in spring and lowered by higher wind stress curl during the rest of the year. The atmospheric bridge that connects the equator and the extratropics has a time lag of about a season (Alexander et al. 2002), which explains the amplification of the warming during the boreal summer.

The increase in wind stress curl along the equator is due to the cooling in the subtropics and warming in the Tropics. It leads to an average strengthening of the equatorial upwelling by about 10% that is strongest during boreal summer.

A La Niña state is amplified by the Bjerknes feedback; a cold anomaly in the eastern equatorial Pacific leads to an increase in the strength of the trade winds. This leads to more upwelling and even colder temperatures. As discussed by Timmermann and Jin (2002), biologically induced surface heating can amplify the warming through the Bjerknes feedback. In our model the Bjerknes feedback is not strongly excited since the induced SST anomalies are too far east of the convection. Compared to a clear water (23-m attenuation depth) experiment, Timmermann and Jin (2002) find an additional heating of 0.55°C month^{-1} from heat absorption by phytoplankton and the indirect effect of the mixed layer depth. In our experiment the MLD shoals by no more than 3 m and the direct heat absorption is also of minor importance.

In our experiment, we find a reduction in the strength of interannual SST variability by about 10%–15%. The skewness and phase locking to the annual cycle are also improved. The ENSO spectral peak is broader than in the fixed ocean, and the dominant ENSO period is increased to around 5 yr. We would again like to note that in this experiment we cannot clearly separate the "interactive biology" effect from the total changes in the variability.

Like Shell et al. (2003), we find that temperature changes also occur over land, where they are often larger than over the ocean. The warming in summer and the change in the seasonal cycle influence large parts of the Northern Hemisphere. There is also a significant cooling over parts of Asia and North America in winter. Changes in sea ice influence large areas in Siberia and Alaska in autumn.

All of these changes lead to the conclusion that the influence of marine biota on the radiative budget of the upper ocean should be considered in detailed simulations of the earth's climate. It is a part of the climate system that is important for the seasonal cycle. There are also indications in this experiment that the interaction of marine biota with the physical system may influence some of the observed interannual and decadal variability in the Pacific, but a detailed exploration of such complex behavior will require longer time series and additional sensitivity studies.

Acknowledgments. We thank Iris Kriest for the help with the biological model and Erich Roeckner, Katja Lohmann, Francisco Alvarez-Garcia, and Robin Smith for valuable comments on the manuscript. This work was funded by the EU Grant EVK2-CT-2001-00134 "Northern Ocean-Atmosphere Carbon Exchange Study," the EU Grant EVK2-1999-00227 "IRONAGES," and the EU Grant GOCE-003903 "DYNAMITE."

REFERENCES

Alexander, M., I. Blade, M. Newman, J. Lanzante, N.-C. Lau, and J. Scott, 2002: The atmospheric bridge: The influence of ENSO teleconnections on air–sea interactions over the global oceans. *J. Climate,* **15,** 2205–2231.

Chavez, F., P. Strutton, and M. McPhaden, 1998: Biological-physical coupling in the central equatorial pacific during the onset of the 1997–98 El Niño. *Geophys. Res. Lett.,* **25,** 3543–3546.

Cloern, J., C. Grenz, and L. Videgar-Lucas, 1995: An empirical model of the phytoplankton chlorophyll:carbon ratio—The conversion factor between productivity and growth rate. *Limnol. Oceanogr.,* **40,** 1313–1321.

Conkright, M., and W. Gregg, 2003: Comparison of global chlorophyll climatologies: In situ, czcs, blended in situ-czcs and seawifs. *Int. J. Remote Sens.,* **24,** 969–991.

Federov, A. V., and S. G. Philander, 2001: A stability analysis of tropical ocean–atmosphere interactions: Bridging measurements and theory for El Niño. *J. Climate,* **14,** 3086–3101.

Fouquart, Y., and B. Bonnel, 1980: Computations of solar heating of the earth's atmosphere: A new parameterization. *Beitr. Phys. Atmos.,* **53,** 35–62.

Gent, P., J. Willebrand, T. McDougall, and J. McWilliams, 1995: Parameterizing eddy-induced tracer transport in ocean circulation models. *J. Phys. Oceanogr.,* **25,** 463–474.

Heinze, C., A. Hupe, E. Maier-Reimer, N. Dittert, and O. Ragueneau, 2003: Sensitivity of the marine biospheric Si cycle for

biogeochemical parameter variations. *Global Biogeochem. Cycles,* **17,** 1086, doi:10.1029/2002GB001943.

Hibler, W., III, 1979: A dynamic thermodynamic sea ice model. *J. Phys. Oceanogr.,* **9,** 815–846.

Jungclaus, J., and Coauthors, 2006: Ocean circulation and tropical variability in the coupled model ECHAM5/MPI-OM. *J. Climate,* **19,** 3952–3972.

Kalnay, E., and Coauthors, 1996: The NCEP/NCAR 40-Year Reanalysis Project. *Bull. Amer. Meteor. Soc.,* **77,** 437–470.

Kara, A., H. Hurlburt, P. Rochford, and J. O. Brien, 2004: The impact of water turbidity on interannual sea surface temperature simulations in a layered global ocean model. *J. Phys. Oceanogr.,* **34,** 345–359.

Lin, S. J., and R. B. Rood, 1996: Multidimensional flux-form semi-Lagrangian transport. *Mon. Wea. Rev.,* **124,** 2046–2068.

Maier-Reimer, E., 1993: Geochemical cycles in an ocean general circulation model: Preindustrial tracer distribution. *Global Biogeochem. Cycles,* **7,** 645–677.

——, I. Kriest, J. Segschneider, and P. Wetzel, 2005: The HAMburg Ocean Carbon Cycle Model HAMOCC5.1—Technical description release 1.1. Rep. 14, Max Planck Institute for Meteorology, Hamburg, Germany, 57 pp. [Available online at http://www.mpimet.mpg.de.]

Manizza, M., C. Le Quéré, A. Watson, and E. T. Buitenhuis, 2005: Bio-optical feedbacks among phytoplankton, upper ocean physics and sea-ice in a global model. *Geophys. Res. Lett.,* **32,** L05603, doi:10.1029/2004GL020778.

Marsland, S. J., H. Haak, J. H. Jungclaus, M. Latif, and F. Roeske, 2003: The Max-Planck-Institute global ocean/sea ice model with orthogonal curvilinear coordinates. *Ocean Modell.,* **5,** 91–127.

Marzeion, B., A. Timmermann, R. Murtugudde, and F.-F. Jin, 2005: Biophysical feedbacks in the tropical Pacific. *J. Climate,* **18,** 58–70.

Miller, A., and Coauthors, 2003: Potential feedbacks between Pacific Ocean ecosystems and inter-decadal climate variations. *Bull. Amer. Meteor. Soc.,* **84,** 617–633.

Moore, J., S. C. Doney, J. Kleypas, D. Glover, and I. Y. Fung, 2002: An intermediate complexity marine ecosystem model for the global domain. *Deep-Sea Res.,* **49B,** 403–462.

Morel, A., 1988: Optical modeling of the upper ocean in relation to its biogenous matter content (case 1 waters). *J. Geophys. Res.,* **93,** 10 749–10 768.

——, and S. Maritorena, 2001: Bio-optical properties of oceanic waters: A reappraisal. *J. Geophys. Res.,* **106,** 7163–7180.

Murtugudde, R., J. Beauchamp, C. McClain, M. Lewis, and A. Busalacchi, 2002: Effects of penetrative radiation on the upper tropical ocean circulation. *J. Climate,* **15,** 470–486.

Nakamoto, S., S. Kumar, J. Oberhuber, K. Muneyama, and R. Frouin, 2000: Chlorophyll modulation of sea surface temperature in the Arabian Sea in a mixed-layer isopycnal general circulation model. *Geophys. Res. Lett.,* **27,** 747–750.

——, ——, ——, ——, and ——, 2001: Response of the equatorial Pacific to chlorophyll pigments in a mixed-layer isopycnal general circulation model. *Geophys. Res. Lett.,* **28,** 2021–2024.

National Geophysical Data Center, 1988: Digital relief of the surface of the Earth. Data Announcement 88-MGG-02, NOAA, Boulder, CO.

Ohlmann, J., and D. Siegel, 2000: Ocean radiant heating. Part II: Parameterizing solar radiation transmission through the upper ocean. *J. Phys. Oceanogr.,* **30,** 1849–1865.

——, ——, and C. Mobley, 2000: Ocean radiant heating. Part I: Optical influences. *J. Phys. Oceanogr.,* **30,** 1833–1848.

Rayner, N., D. Parker, E. Horton, C. Folland, L. Alexander, D. Rowella, E. Kent, and A. Kaplan, 2003: Global analyses of sea surface temperature, sea ice, and night marine air temperature since the late nineteenth century. *J. Geophys. Res.,* **108,** 4407, doi:10.1029/2002JD002670.

Roeckner, E., and Coauthors, 2003: The atmospheric general circulation model ECHAM 5. Part I: Model description. Rep. 349, Max Planck Institute for Meteorology, Hamburg, Germany, 127 pp. [Available online at http://www.mpimet.mpg.de.]

Shell, K. M., R. Frouin, S. Nakamoto, and R. Somerville, 2003: Atmospheric response to solar radiation absorbed by phytoplankton. *J. Geophys. Res.,* **108,** 4445, doi:10.1029/2003JD003440.

Siegel, D., J. C. Ohlmann, L. Washburn, R. Bidigare, C. Nosse, E. Fields, and Y. Zhou, 1995: Solar radiation, phytoplankton pigments and radiant heating of the equatorial Pacific warm pool. *J. Geophys. Res.,* **100,** 4885–4891.

Six, K., and E. Maier-Reimer, 1996: Effects of plankton dynamics on seasonal carbon fluxes in an ocean general circulation model. *Global Biogeochem. Cycles,* **10,** 559–583.

Strutton, P. G., and F. P. Chavez, 2004: Biological heating in the equatorial Pacific: Observed variability and potential for real-time calculation. *J. Climate,* **17,** 1097–1109.

Sweby, P., 1984: High resolution schemes using flux limiters for hyperbolic conservation laws. *SIAM J. Numer. Anal.,* **21,** 995–1011.

Timmermann, A., and F.-F. Jin, 2002: Phytoplankton influences on tropical climate. *Geophys. Res. Lett.,* **29,** 2104, doi:10.1029/2002GL015434.

Timmreck, C., and M. Schulz, 2004: Significant dust simulation differences in nudged and climatological operation mode of the AGCM ECHAM. *J. Geophys. Res.,* **109,** D13202, doi:10.1029/2003JD004381.

Valcke, S., A. Caubel, D. Declat, and L. Terray, 2003: Oasis ocean atmosphere sea ice soil users's guide. Tech. Rep. TR/CMGC/03/69, CERFACS, Toulouse, France, 85 pp.